Facile in situ generation of bismuth tungstate nanosheet-multiwalled carbon nanotube composite as unconventional affinity material for quartz crystal microbalance detection of antibiotics

Munawar, Anam; Schirhagl, Romana; Rehman, Abdul; Shaheen, Ayesha; Taj, Ayesha; Bano, Khizra; Bassous, Nicole J; Webster, Thomas J; Khan, Waheed S; Bajwa, Sadia Z

Published in:
Journal of hazardous materials

DOI:
10.1016/j.jhazmat.2019.03.054

Publication date:
2019

Journal of Hazardous Materials 373 (2019) 50–59

Contents lists available at ScienceDirect

Journal of Hazardous Materials

journal homepage: www.elsevier.com/locate/jhazmat

Facile in situ generation of bismuth tungstate nanosheet-multiwalled carbon nanotube composite as unconventional affinity material for quartz crystal microbalance detection of antibiotics

Anam Munawar[a,b,c], Romana Schirhagl[b], Abdul Rehman[d], Ayesha Shaheen[a,c], Ayesha Taj[a,c], Khizra Bano[a,c,e], Nicole J. Bassous[e], Thomas J. Webster[e], Waheed S. Khan[a,f,**], Sadia Z. Bajwa[a,*]

[a] National Institute for Biotechnology and Genetic Engineering (NIBGE), P.O. Box No.577, Jhang Road, Faisalabad, Pakistan
[b] University of Groningen, University Medical Center Groningen, Department of Biomedical Engineering, Antonius Deusinglaan 1, 9712AW Groningen, Netherlands
[c] Pakistan Institute of Engineering and Applied Sciences, Nilore, Islamabad, Pakistan
[d] Chemistry Department, King Fahd University of Petroleum and Minerals (KFUPM), Dhahran 31261, Saudi Arabia
[e] Department of Chemical Engineering, Northeastern University, Boston, MA, USA
[f] Nanobiomaterials Group, Ningbo Institute of Materials Technology and Engineering (NIMTE), Chinese Academy of Sciences (CAS), Ninbgo City, Zhejiang, China

GRAPHICAL ABSTRACT

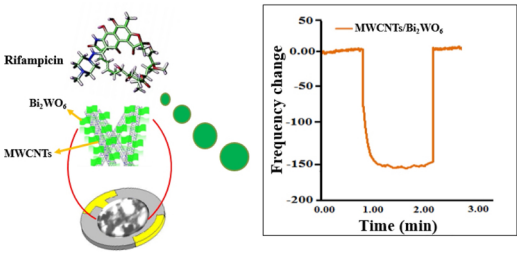

ARTICLE INFO

Keywords:
Hybrid materials
Quartz crystal microbalance
Bismuth tungstate
Multiwalled carbon nanotubes

ABSTRACT

Overuse and thus a constant presence of antibiotics leads to various environmental hazards and health risks. Thus, accurate sensors are required to determine their presence. In this work, we present a mass-sensitive sensor for the detection of rifampicin. We chose this molecule as it is an important antibiotic for tuberculosis, one of the leading causes of deaths worldwide. Herein, we have prepared a carbon nanotube reinforced with bismuth tungstate nanocomposite material in a well-defined nanosheet morphology using a facile in situ synthesis mechanism. Morphological characterization revealed the presence of bismuth tungstate in the form of square nanosheets embedded in the intricate network of carbon nanotubes, resulting in higher surface roughness of the nanocomposite. The synergy of the composite, so formed, manifested a high affinity for rifampicin as compared to the individual components of the composite. The developed sensor possessed a high sensitivity toward rifampicin with a detection limit of 0.16 μM and excellent specificity, as compared to rifabutin and rifapentine. Furthermore, the sensor yielded statistically good recoveries for the monitoring of rifampicin in human urine samples. This work opens up a new horizon for the exploration of unconventional nanomaterials bearing different morphologies for the detection of pharmaceuticals.

* Corresponding author.
** Corresponding author at: National Institute for Biotechnology and Genetic Engineering (NIBGE), P.O. Box No.577, Jhang Road, Faisalabad, Pakistan.
E-mail addresses: waheedskhan@yahoo.com (W.S. Khan), sadya2002pk@yahoo.co.uk, sadia.zafar.bajwa@gmail.com (S.Z. Bajwa).

https://doi.org/10.1016/j.jhazmat.2019.03.054
Received 5 March 2018; Received in revised form 4 March 2019; Accepted 12 March 2019
Available online 18 March 2019
0304-3894/

1. Introduction

The increasing drug market binds pharmaceutical companies to have strict regulations to ensure quality and stability for appropriate formulations of designed drug [1]. In this context, the selective and sensitive detection of drugs is of high demand based on their clinical importance. Particularly important is the detection of antibiotics as their overuse and constant presence (especially at lower concentrations) leads to the evolution of resistant bacterial strains which cannot be killed any more by antibiotics. Being one of the top 10 causes of deaths worldwide, tuberculosis is arguably the most important disease to target. This situation gets worse as about 480,000 people were reported to develop multidrug-resistant tuberculosis merely in 2015 [2,3]. In this connection, rifampicin (RIF) is an important drug as it is widely used in the treatment of bacterial infections to treat or prevent tuberculosis [4]. Although, the rifamycins include rifampicin, rifapentine, and rifabutin. Of these, rifampicin is most commonly used, either as first-line therapy (in combination with other agents) for treatment of mycobacterial disease (including tuberculosis). In contrast, rifabutin is used in those patients who cannot tolerate rifampicin. While rifapentine is less preferred due to hepatotoxicity [5]. Therefore, rifampicin is arguably the most important drug in the treatment of tuberculosis (TB). Stability studies showed that rifampicin is stable in the blood and urine for only a few hours. Blood plasma or urine can be used as a matrix to check for the presence of rifampicin [6].

Rifampicin basically inhibits bacterial DNA-dependent RNA synthesis by inhibiting bacterial DNA-dependent RNA polymerase [7]. More common side effects include fever, gastrointestinal disturbances, rashes, and immunological reactions [8]. Although the drug has been administered for many decades, but there are still questions about the appropriateness of dosage regimes, especially in specific patient groups such as those co-infected with HIV and young children [9]. In order to address these health concerns, there is a stringent need to develop suitable selective and sensitive analytical method, contrary to equipment based expensive techniques like high performance liquid chromatography (HPLC), enzyme linked immune sorbent assay (ELISA), interferometric reflectance imaging sensor (IRIS) [10–12].

We decided to use nanostructured tungstate for sensor development due to its remarkable electrical conductivity (10^{-7} to 10^{-3} S cm^{-1}) [13,14]. Among the metal tungstate, bismuth tungstate (Bi_2WO_6) takes precedence due to its high chemical stability, higher catalytic activity, as well as molecular and electronic versatility. This material has been explored extensively and has excellent performance for nonlinear dielectric susceptibility [15], acoustic insulators [16], ferroelectric [17], efficient catalysts [18], pyro electricity [19], photonic building blocks [20], oxide anion conducting [21], piezoelectricity [22], photocatalytic activity [23,24], decontamination [25], sustaining drug releasing agents [26], *etc*.

Carbon nanotubes (CNTs) offer remarkable physical and chemical properties owing to their small dimensions, strength, and other special structural features. Generally, CNTs have been applied in sensing devices and in particular electrochemical biosensors [27,28]. CNT-based transducers offer substantial improvements in the performance of electrochemical sensors, immunosensors, and nucleic-acid sensing devices [29]. Apart from sensing applications [30] they are also valued in nano-electronics or as tips for scanning probe microscopes, photo catalysts [31], gas storage materials [32], strength enhancing materials [33], composite materials [34], in self-healing technologies [35], and drug delivery [36]. The properties of CNTs can be ameliorated by their association with other forms of nanomaterials, where, the resultant synergy can produce very exciting nanomaterials with interesting properties [37].

A quartz crystal microbalance (QCM) as a transducer element constitutes a robust and sensitive detection platform [38]. Furthermore, the technology can be adapted to various applications by altering the electrode geometry or the electrode material and hence a large variety of coating materials allow for sensitive monitoring of various analytes in real time [39,40]. Conventionally, either bare QCM electrodes are employed or the electrodes are coated with metal nanoparticles of varying morphologies or polymer films. However, the use of nanocomposite as a transducer layer over QCM is a less explored area [41].

In the present study, we introduce an entirely new and an innovative way to prepare unconventional nanomaterials with unique morphology for mass sensitive detection of antibiotics. To the best of our knowledge, this is the first report about the synthesis and investigation of MWCNTs and bismuth tungstate nanosheets, for mass-sensitive measurements. We designed this study focusing many aspects (i) in situ development of 2D Bi_2WO_6 nanosheets onto 1D CNTs, (ii) to study whether if such composite can be used as a QCM transducer, in contrast to traditional smooth layers, and (iii) to evaluate 1D CNTs and 2D Bi_2WO_6 composite for the real-time monitoring of RIF, where electrostatic interactions have played the main directive force to generate selectivity. On one hand, the development of a material is studied, whereas the synergy effects of MWCNTs and bismuth tungstate nanosheets as a transducer material of QCM are explored. This allowed for the label-free, real-time detection of the RIF drug with high sensitivity and selectivity in comparison to other drugs of similar chemical nature and function. This work opens up new avenues to prepare exceptional nanomaterials of different morphologies than conventional materials.

2. Materials and methods

2.1. Chemicals and apparatus

All chemicals were purchased either from Merck or Sigma–Aldrich. These were of analytical reagent grade or of higher available synthetic grade and were utilized without further purification. MWCNTs with an average outer diameter of 25–50 nm and 10–15 μm of average length were provided by Shenzhen Nanotech Port. Co. Ltd. All solutions were prepared using ultrapure water (ρ = 18 MΩ cm) from a Millipore-Milli Q system. Rifampicin (RIF) capsules were purchased from Merck & Co. This drug was used without further purification. All the solutions and modified QCM devices were stored at room temperature when not in use.

2.2. Preparation of MWCNTs-Bi_2WO_6 nanocomposite (MWCNTs/Bi_2WO_6)

First CNTs were functionalized to possess amine groups. In a typical preparation, 0.03 g of MWCNTs were dispersed in polyethylenimine (1% v/v) followed by sonication for about 2 h. After keeping them at room temperature for 12 h and removing excess PEI, MWCNTs were dispersed in 40 mL of methanol to produce a stable colloid. Afterwards, a freshly prepared (20 mL of 2.5 M in acetic acid) solution of Bi $(NO_3)_3{\cdot}5H_2O$ was added, followed by the drop wise addition of the aqueous solution of $Na_2WO_4{\cdot}2H_2O$ (5 mL of 0.05 M). Afterwards, it was centrifuged, rinsed with 5 mL each of methanol and H_2O, and dried under vacuum at 50 °C. Finally, the obtained product was stored in desiccators.

The stock solution of RIF was prepared in 1 M dimethyl sulfoxide (DMSO) and further dilutions of this solution were prepared in phosphate buffer saline (pH 7.4), when required. To investigate selectivity, the stock solutions of rifabutine (RIB) and rifapentine (RIP) were prepared and diluted in the similar way.

2.3. Characterization of nanomaterials

The morphology of MWCNTs and MWCNTs/Bi_2WO_6 nanocomposite was studied with a field emission scanning electron microscope (FESEM) (JSM-7500F-JEOL, Japan). For this purpose, each of these materials were dispersed in deionized water (1 mg mL^{-1}) and 10 μL out of this dispersion were dropped onto carbon coated copper grids (200 mesh).

Atomic force microscope (AFM) (SHIMADZU WET-SPM 9600, Japan) was used to study surface and related roughness parameters (RMS). To prepare samples, 10 µL out of the above prepared suspensions were coated onto a 0.5 cm^2 glass support for AFM analysis. Three samples of each material were imaged for at least three different areas using the same tip. To get scans, silicon nitride atomic force microscopy (AFM) probes (model OMCL-TR800PSA-1) having micro cantilevers, 100 µm thickness and force constants of 0.57 N m^{-1} were used. All the scans were carried at ambient temperature in contact mode. For the data analysis, software (SPM Manager) provided by the AFM system supplier was used. The same software was applied to calculate surface roughness parameters for all of the prepared materials.

Powder X-ray diffraction (P-XRD) spectra of the MWCNTs/Bi_2WO_6 nanocomposite were recorded using a X'pert Pro PAN analytical (Germany) diffractometer using monochromatic CuKα radiation (λ = 1.5406 A) operating at 40 kV and a current of 30 mA. The data for the nanocomposite were collected over a range of 10–80° 2θ.

Dynamic light scattering (DLS) experiments were carried out to determine the surface charge of MWCNTs/Bi_2WO_6 nanocomposite. For that purpose, a Zeta Sizer (Nano-ZS; Malvern Instruments) with its software, Dispersion Technology Software (DTS) was used.

For FTIR qualitative analysis, materials were studied using the horizontal attenuated total reflectance (HAT) mode of a FTIR spectrometer (PerkinElmer Frontier™ with Touch™ software). To acquire spectra, a premium HATR plate with flat top and fitted with a ZnSe 45° crystal was used as it allows for simple sampling of solids, polymer films, and powders. This equipment provides one method of measuring the IR spectra in transmission with relatively long pathlength and, together with C-H bands, thus gives the greatest sensitivity. To obtain profiles, 0.5 mg of the MWCNTs and MWCNTs/Bi_2WO_6 nanocomposite were dissolved in 1 mL of methanol. To study the functional groups of RIF, and interaction of nanocomposite with RIF (MWCNTs/Bi_2WO_6-RIF), RIB (MWCNTs/Bi_2WO_6-RIB), and RIP (MWCNTs/Bi_2WO_6-RIP), 500 µL of each drug (0.5 mM in DMSO) was mixed with 10 µL of the composite suspension (1 mg mL^{-1} in methanol).

2.4. Quartz crystal microbalance measurements

The QCM200 System consists of a thin AT-cut, α-quartz disk of 5 MHz, 1 inch in diameter, with circular gold electrodes (100–1000 mm thick coating). Circular electrodes were patterned on both sides, i.e. front side (12 mm diameter for the liquid surface) and on the rear side (5 mm diameter for the electrical contact purpose). The large diameter of the crystal, and the relatively much smaller oscillation area, assures good separation between the active electrode pads and the mounting structure of the holder. This minimizes the coupling of other resonant modes to the thickness shear oscillation as well.

The exposed area of the front electrode in contact with the liquid is ~1.37 cm^2, however, the active electrode oscillation (i.e. displacement area) is mostly restricted to ~0.40 cm^2. This extremely sensitive sensor is capable of measuring mass changes in the ng/cm^2 range with a wide dynamic range extending into the 100 µg/cm^2 range [42].

2.5. Preparation of QCM devices

Before modification, all QCM devices used in this study were cleaned by piranha solutions (a mixture of 3:1 sulfuric acid and 30% hydrogen peroxide) to remove residues from the substrate. After washing, 10 µL of MWCNTs/Bi_2WO_6 nanocomposite dispersion (1 mg mL^{-1}) in methanol was drop-coated. By spinning the substrate (speed 1000 RPM; 15 s) the droplet was forced to spread out while the solvent evaporated. The resultant device was dried at 60 °C for 3 h and then at room temperature for 24 h. Following this procedure, a very thin layer of MWCNTs/Bi_2WO_6 of about 18–20 nm on the quartz crystal was achieved (calculated by AFM).

2.6. Mass-sensitive measurements

The modified QCM device was mounted in a crystal holder's head on a flat surface, with its crystal cavity pointing up. The crystal cavity contains two spring-loaded contacts (POGO® pins), which connect the two contact surface circuits of the crystal to the BNC connector on the opposite end of the probe. The device was exposed to the desired concentration of analyte in batches through a series of load/rinse exchanges. This was further connected to frequency, output port (BNC) on the front panel for connection to an external frequency counter. For data acquisition and storage, SRS QCM200 software was used. All mass changes were observed in terms of frequency shifts as a function of time, at 25 ± 2 °C with three separately MWCNTs/Bi_2WO_6 modified QCM devices. All solutions for sensor measurements were prepared in phosphate buffer saline and the required concentrations were obtained by the appropriate dilutions of the respective stock solutions.

3. Results and discussion

3.1. Characterization of MWCNTs/Bi_2WO_6 nanocomposite

The overall process for the fabrication of MWCNTs and the Bi_2WO_6 nanocomposite is schematically depicted in Fig. 1. In order to generate in situ, a facile method was carried out that is in itself improved than many reported procedures [43–47] for the synthesis of different nanostructures of bismuth tungstate. The facile and cost-efficient growth

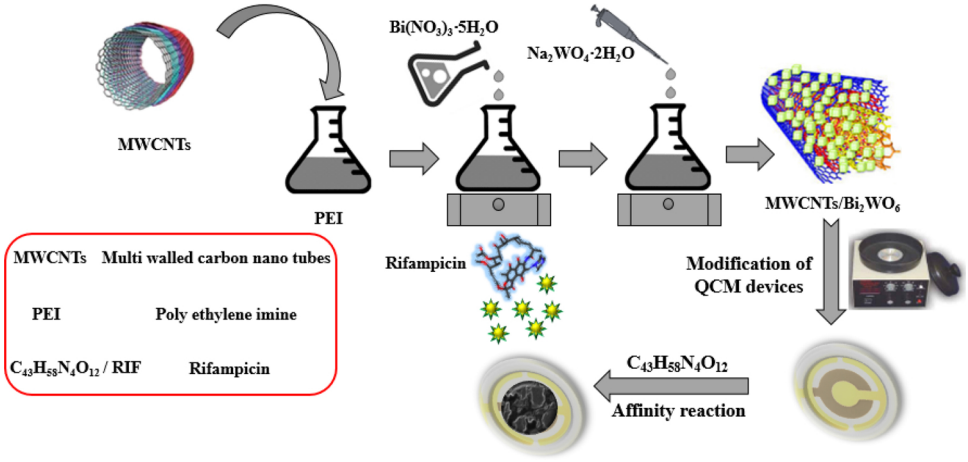

Fig. 1. Schematic illustration for designing MWCNTs/Bi_2WO_6 nanocomposite for the detection of rifampicin.

of nanosheets bears much significance when very expensive methods like chemical vapor deposition techniques are in vogue [12,48]. Moreover, the process of migration of growing seeds on another support is very important to develop composite nanosheets [49]. We have carried out their successful in situ self-seeding growth in presence other structures like CNTs a very facile, solution based method. The applications of CNTs in general, and specifically as sensor transducer material, are considerably limited by their negligible suspension into aqueous and milder organic solution owing to the powerful intermolecular van der Waals bonds between tubes resulting in agglomerations [50]. To produce stable dispersion and to provide active centers for the growth of sheets over tubes, in the first, step carbon nanotubes were functionalized to furnish amine group. Amine modified CNTs have been studied since the amine group has great reactivity and can interact and allow for the adsorption of bismuth tungstate sheet on its modified surface. In the second step, bismuth salt was introduced, presumably making a complex with amine moieties of CNT/PEI dispersion. When the tungstate salt was added, it resulted in the formation and deposition of Bi_2WO_6 nanosheets. In fact, bismuth tungsten oxide grows in supersaturated $Bi(NO_3)_3$ and Na_2WO_4 solutions, and fine seed particles can act as the precursor to deposit nanosheets [51]. Such direct deposition of the nanomaterial over the CNTs is more suitable for sensor applications because of the better distribution of material characteristics over the network of nanotubes.

The size, shape, and morphology of the MWCNTs/Bi_2WO_6 nanocomposite were studied by recording FESEM images (Fig. 2A and B) which actually provides a comparison of CNTs alone and the CNTs with deposited Bi_2WO_6. Morphologies are significantly different in the two images. Bi_2WO_6 sheets can be seen embedded in the network of MWCNTs strands in Fig. 2B. The diameter of MWCNTs was about 20–25 nm whereas, nanosheets were ~100–200 nm in length and of similar dimension in width. Based on these observations, it was concluded that the prepared composite sheets are square shaped. After the formation of the composite, the network became more crowded and entangled due to the presence of nanosheets. FESEM in TEM mode images (Fig. 2C and D) further confirmed the presence of square shaped nanosheets anchored on the tubular structures of CNTs.

MWCNTs and the MWCNTs/Bi_2WO_6 nanocomposite were characterized by AFM and the resulting representative topographies are displayed in Fig. 3. Here, the strands of MWCNTs (about 25 nm) can be seen (Fig. 3A). However, after the formation of the composite, the height and width of the nanotubes were increased to about 50–100 nm (Fig. 3B). This can be credited to the agglomeration of Bi_2WO_6 nanosheets over their surface which is shown as an increase in AFM height. The dimensions of sheets were estimated to be 100–200 nm in length and width. The height of the sheets was found to be 1–2 nm which validates the sheet structures of Bi_2WO_6, after the formation of the composite (Fig. 3C and D). However, at various places, the sheets were stacked in bundles of ~100–500 nm, embedded in the intricate network of MWCNTs. The surface roughness parameter (RMS) for MWCNTs was calculated to be 15 nm, where its value for the MWCNTs/Bi_2WO_6 nanocomposite was 35 nm. This high increase in roughness clearly indicated the surface modification of MWCNTs. Comparing Figs. 2 and 3, we found that AFM images are in good agreement with FESEM and TEM results, in turn corroborating the surface modification of MWCNTs by the formation of the MWCNTs/Bi_2WO_6 nanocomposite.

The phase structure, crystallinity, and purity of the as-obtained Bi_2WO_6 nanosheets over MWCNTs were examined by XRD measurements. Fig. 4A is depicting the XRD pattern of the MWCNTs/Bi_2WO_6 nanocomposite, different characteristic peaks at 25°, 28.3°, 32°, 46° and 55° correspond to the (002), (113), (200), (220) and (313) inter-planar spacing of MWCNTs and Bi_2WO_6 nanosheets, respectively. No peaks of

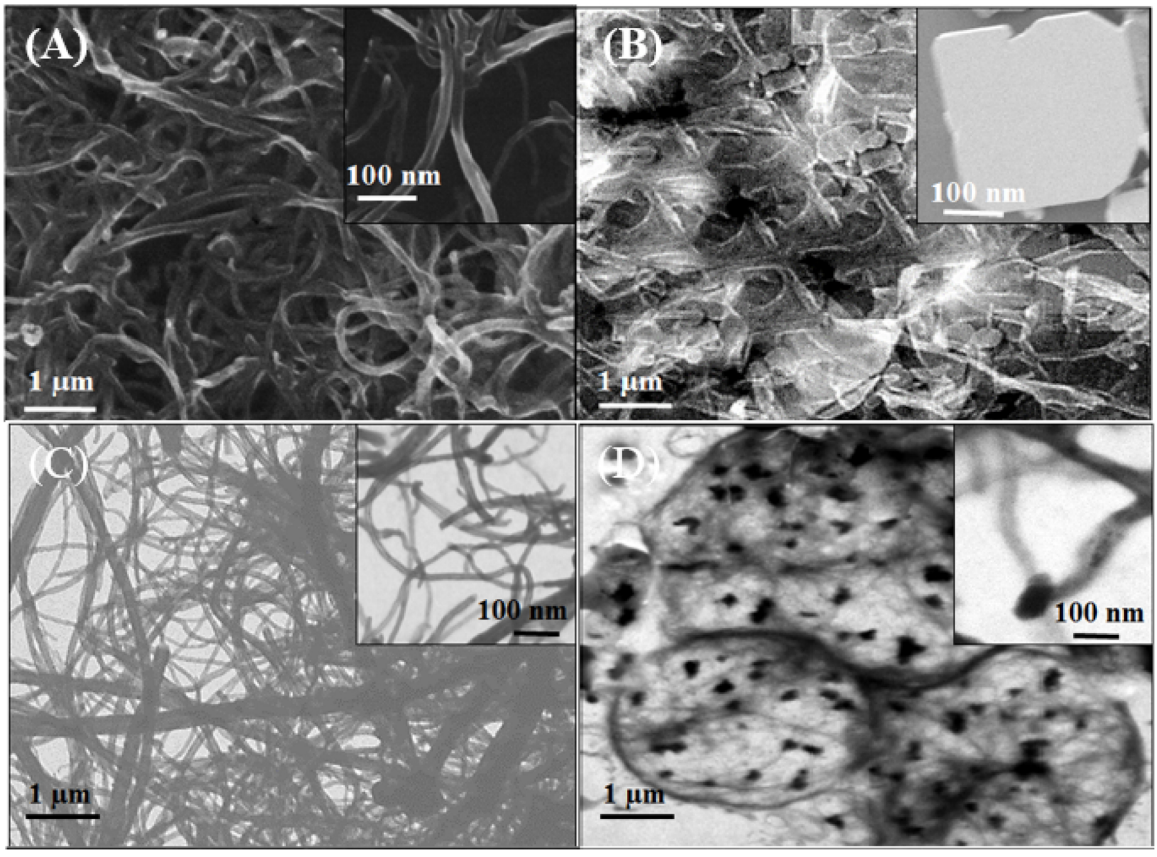

Fig. 2. Morphological Characterization (A) SEM images showing the morphology of MWCNTs, (B) MWCNTs/Bi_2WO_6 nanocomposite, inset is showing the Bi_2WO_6 nanosheets, (C) TEM images of MWCNTs and (D) MWCNTs/Bi_2WO_6 nanocomposite; inset is showing the Bi_2WO_6 nanosheets anchored on the strands of MWCNTs.

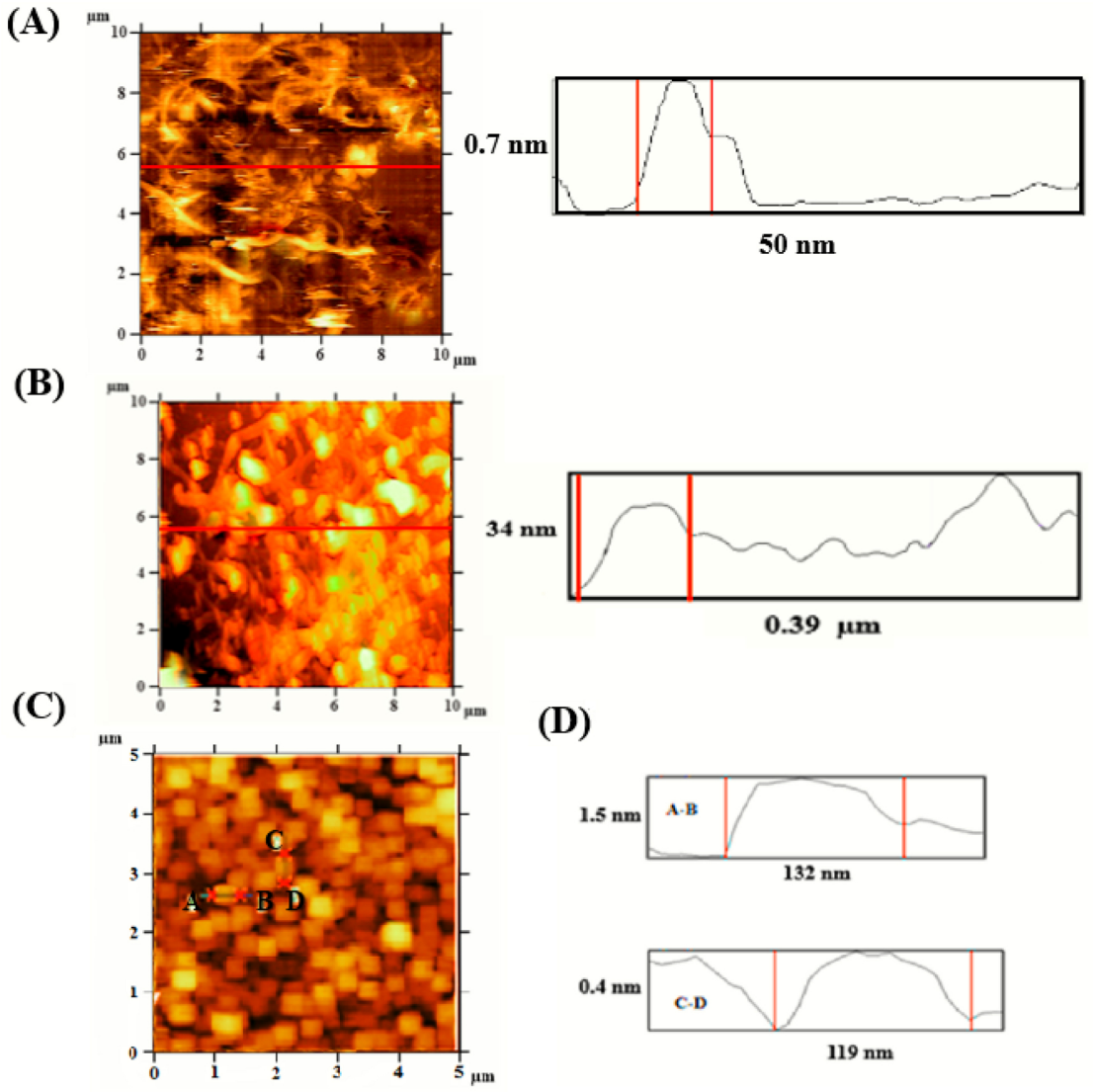

Fig. 3. Surface characterization (A) AFM images showing morphology of MWCNTs, (B) MWCNTs/Bi_2WO_6 nanocomposite, (C) Bi_2WO_6 nanosheets, and (D) profile showing the height and width of nanosheets. For these experiments, the parameters are scan size = 10 µm and 5 µm, scan rate = 1 Hz, image data = height and sample lines = 512.

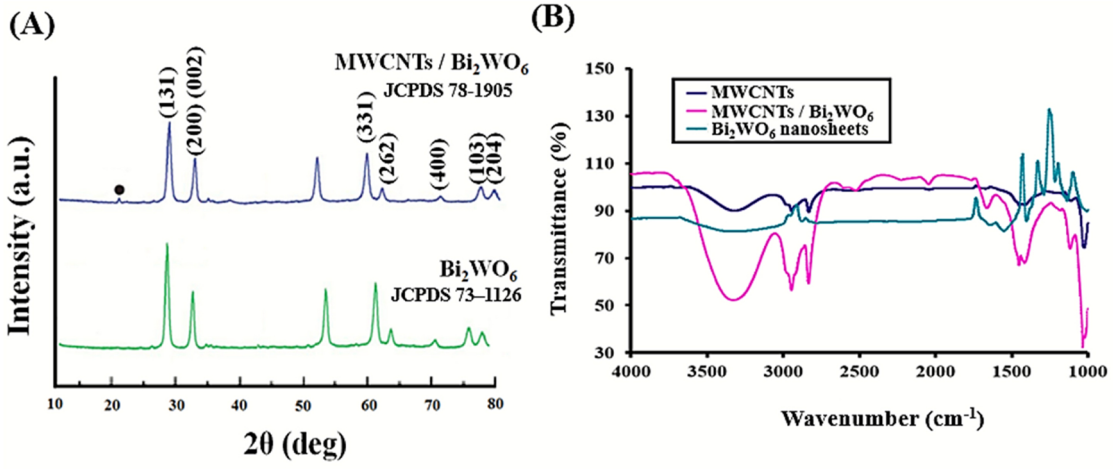

Fig. 4. Structural characterization (A) XRD patterns for Bi_2WO_6 and MWCNT/Bi_2WO_6 nanocomposite and (B) HATR-IR profiles of the MWCNTs, Bi_2WO_6 nanosheets and MWCNTs/Bi_2WO_6 nanocomposite.

other impurities are detected, indicating the purity of the products. The wide diffraction peaks show that the size of the crystalline grain is small. The average crystalline size estimated from the (131) peak is about 80 and 120 nm, according to the Scherrer equation for samples and MWCNTs/Bi_2WO_6 nano-architectures. In the XRD pattern of MWCNTs/Bi_2WO_6 nanocomposite, all characteristic peaks of Bi nanosheets are present, which strongly validates the loading of the Bi_2WO_6 nano-sheets on MWCNTs surface.

Fig. 4B shows the HATR-IR spectra of the MWCNTs, Bi_2WO_6 and MWCNTs/Bi_2WO_6 from 1000 to 4000 cm^{-1}. In the case of MWCNTs, the spectrum showed a broad peak at 3349 cm^{-1} which represents the presence of CH—H. The presence of a noticeable band at 1414 cm^{-1} corresponds to the C—H stretching. While in case of pure Bi_2WO_6 nanosheets, no bands were observed. If we compare the IR profile of the nanocomposite with that of MWCNTs, we can see that main backbone of carbon is consumed during the formation of the composite. In fact, MWCNTs can adsorb PEI (cationic polyelectrolyte) due to electrostatic interactions. A large number of imine groups present on the PEI polymer chain can coordinate with the $Bi(NO_3)_3{\cdot}5H_2O$ salt. With the addition of ($Na_2WO_4{\cdot}2H_2O$), it leads to the formation Bi_2WO_6 nanosheets [52]. The change of this carbon, carbon network of CNTs occurred as the result of the modification of the CNT backbone (—C—C—) with PEI and further by the formation of nanosheets.

The mechanism of the reaction was further supported by investigating zeta-potentials. The respective zeta potential graphs of Bi_2WO_6 nanosheets and nanotubes wrapped with Bi_2WO_6 are displayed in Fig. S1 (supplementary information). Bi_2WO_6 plain nanostructures possessed a positive potential (1.8 mV) in contrast to MWCNTs wrapped with Bi_2WO_6 which showed a negative potential (−18.5 mV). This change of surface charge can be attributed to the presence of a MWCNTs network that holds an inherent negative charge.

3.2. Basic sensor signals

Mass-sensitive measurements were carried out by recording the frequency responses of bare and different modified QCM devices, Bi_2WO_6 nanosheets, MWCNTs, and MWCNTs/Bi_2WO_6 nanocomposite, toward 0.5 mM of RIF. The resultant sensor signals are displayed in Fig. 5A. MWCNTs/Bi_2WO_6 showed a response of 150 ± 0.02 Hz as compared to the bare gold electrode exhibiting a frequency shift of 25 ± 0.02 Hz. The significantly higher net sensor response (125 Hz) shown toward RIF template as compared to the bare gold signifies the capability of the prepared nanocomposite toward the detection of the RIF. The increase of sensor responses due to the use of MWCNTs and Bi_2WO_6 alone has also been calculated. The coatings prepared by individual MWCNTs displayed a response of 50 ± 0.02 and if we compare that with the frequency shift of the nanocomposite, the resultant 100 Hz advocates the strength of using MWCNTs for the composite synthesis. This increase in sensor response is due to the addition of MWCNTs which can be expressed as the *composite effect*. The enhancement of sensor response due to a combination of CNTs and Bi_2WO_6 nanosheets, can also be calculated as the sensor layer of plain Bi_2WO_6 nanosheets generating a 46 ± 0.02 Hz frequency shift, which means a net sensor response of 104 Hz. Undoubtedly, this improvement in sensor response is the result of *collaborative effects* produced by MWCNTs and Bi_2WO_6. This can be assigned as a *synergistic factor*. This not only improves the surface properties as accessibility and diffusion, which in turn affects the affinity interactions of RIF with the sensor layer.

The highest increase of sensor response by the use of the composite was supported by the HATR-IR studies (Fig. S2) where the peaks within the 2000–1000 cm^{-1} wavelength can be assigned due to the interaction of RIF with the composite. Fig. S2 of the HATR-IR of rifampicin showed an absorption band within the region of 2807 to 3699 cm^{-1} corresponding to CH—H, =C—H and OH bonds [53]. The broadened shape of the band indicates the greater number of these chemical moieties. The characteristic sharp peaks at about 1727 cm^{-1} for acetyl C=O, at 1649 and 1562 cm^{-1} representing the C=O of furanone and C=O of amide group, respectively [54]. These bands were found in areas of major changes as the result of interaction of nanocomposite with RIF. Here, the HATR-IR spectra of the suspension showed a strong transmission at 2942 for aromatic C—H and at 2829 cm^{-1} for aldehyde C—H stretch, and a distinct sharp band was observed at 1416 cm^{-1} for alkane C—H [55]. It can be assumed that the carbonyl moieties of the assorted chemical nature present in RIF might have interacted with the composite, which in turn resulted in higher frequency shifts, when used as a QCM transducer layer.

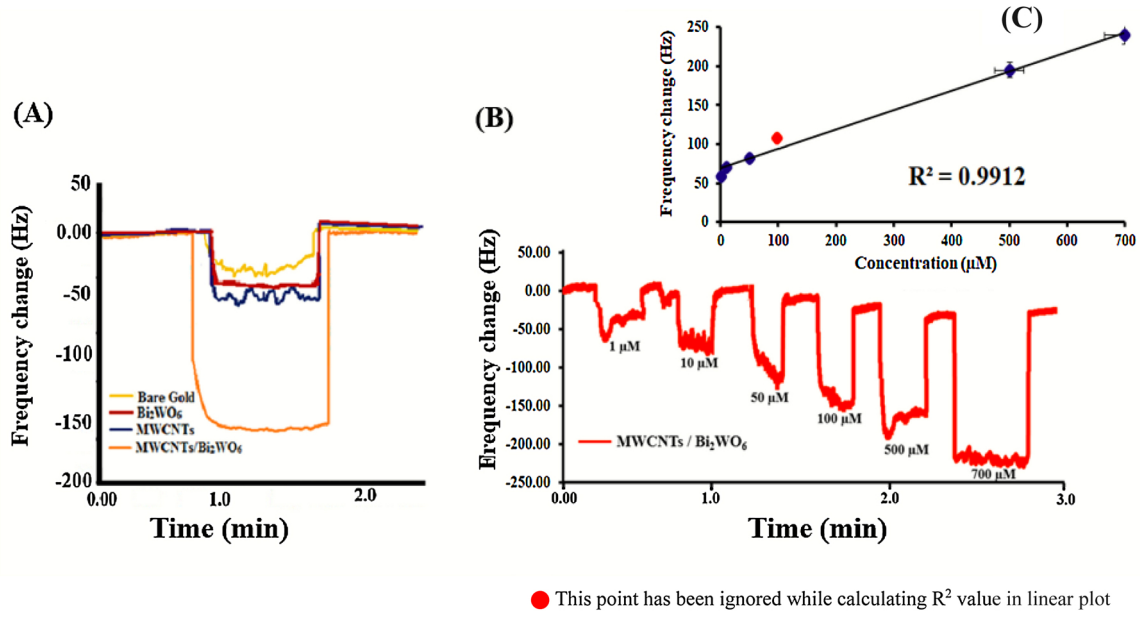

Fig. 5. Sensor characteristics (A) QCM sensor signals of bare gold, Bi_2WO_6 nanosheets, MWCNTs and MWCNTs/Bi_2WO_6 modified electrodes toward 0.5 mM rifampicin, (B) Frequency shift profile of MWCNTs/Bi_2WO_6 modified QCM device toward rifampicin (0.001–0.7 mM), in PBS (pH = 7.4); inset (C) is showing the calibration curve with regression value.

3.3. Analytical performance

Since the designed composite exhibited a greater response toward RIF, further analytical parameters were studied by exposing the modified QCM devices to varying concentrations of RIF (from 0.001 mM to 0.7 mM). Fig. 5B reveals the steady increase of frequency shift with increasing concentrations of rifampicin. The corresponding decrease in frequency was found to be statistically significant. The correlation between the frequency shifts due to mass accumulation on the surface is attributed to the interaction of RIF molecules with the composite. It strongly indicates affinity interactions based detection of RIF when the MWCNTs/Bi_2WO_6 nanocomposite is used as a receptor. The linear sensor characteristics were found to have a correlation coefficient of $R^2 = 0.9912$. Two important analytical parameters are LoD (lower limit of detection) and LoQ (lower limit of quantification) are studied. To calculate the LoD and LoQ, the following formulas were used:

$$\text{LoD} = 3.3\sigma/\text{Slope}$$

$$\text{LoQ} = 10\sigma/\text{Slope}$$

where: σ = the standard deviation of the response at low concentrations, Slope = the slope of the calibration curve.

The slope may be estimated from the calibration curve of the analyte. The estimate of σ is typically the root mean squared error (RMSE) or standard deviation of the residuals taken from the regression line. The limit of detection was estimated to be 0.16 µM (S/N = 3) whereas, the limit of quantification was 0.50 µM. This demonstrates exceedingly high sensitivity of the designed sensor as compared to other reported sensors for detection of RIF as shown in Table 1 [56–60].

3.4. Repeatability and stability

Two further key parameters for the practical usefulness of sensors are stability and ruggedness: to assess these, we exposed sensors by recording three experiments of equilibration and regeneration cycles to 0.5 mM of RIF. The resulting frequency signals are displayed in Fig. S3. First of all, signals are stable. Moreover, each cycle is achieved with statistically significant regeneration. It showed that the prepared composite yielded sensor coatings that can be used for the reliable detection of RIF.

To investigate long term stability, we exposed the prepared devices toward 0.5 mM RIF at different days, i.e. sensor measurements were recorded at the 1st day, and then after two weeks. During time intervals, the devices were stored at room temperature. The resultant sensor responses are shown in Fig. S4. The values of frequency were calculated to be 152 ± 0.03 and 150 ± 0.02, which means only a very small loss of mass from the surface coating. It indicates that the MWCNTs/Bi_2WO_6 nanocomposite QCM sensors are highly stable, when used for the detection of the drug.

Table 1
Comparison of sensor analytical parameters with already reported methods for the detection of RIF.

Serial no.	Method	Device	LoD (µM)	Reference
1	Amperometry	β-Cyclodextrin/polypyrrol platinum electrode	1.69	[56]
2	SWAdSV	DyNW/CPE	0.5	[57]
3	LSV	$Ni(OH)_2$–RGO	4.16	[58]
4	DPP	HMDE	10	[59]
5	EIS and CV	PMel-Au nanocomposite	0.03	[60]
6	QCM	MWCNTs/Bi_2WO_6	0.16	This work

Square-wave adsorptive stripping voltammetry (SWAdSV); dysprosium nanowires modified carbon paste electrode (DyNW/CPE); nickel hydroxide nanoparticle-reduced graphene oxide nanosheets ($Ni(OH)_2$–RGO); linear sweep voltammetry (LSV); differential pulse polarographic (DPP); hanging mercury drop electrode (HMDE); electrochemical impedance spectroscopy (EIS) and cyclic voltammetry (CV); poly-melamine/gold nanoparticles nanocomposite (PMel-Au).

3.5. Selectivity

The cross-sensitivity of the prepared QCM devices was also investigated. Binding features or inherent material interactions can be implemented to design artificial receptor matrices [29,61]. In this respect, a range of different non-covalent interactions can be employed depending on the chemical properties of the respective analyte, such as affinity-based ones, hydrophobic interactions, hydrogen bonds, and polar interactions [30]. Obviously, the interactions between the analyte and matrix play a key role in controlling the recognition ability of the material in any case [32]. In our study, we have used electrostatic interactions between the MWCNTs/Bi_2WO_6 composite and RIF as the directing or driving force. We have emphasized that the resulting selectivity should be influenced by the nature and extent of mutual interactions. For this purpose, we selected a couple of drugs which are very similar in their actions to RIF and are alternatively used to treat various infections. We took a systematic approach in the way that one of the drugs chosen for this study was very similar in structure to RIF, i.e. rifapentine (RIP) with the notable substitution of a methyl group for a cyclopentane (C_5H_9) group.

Rifabutin is an antibiotic which is used to treat tuberculosis and to prevent the tuberculosis complex. It is typically only administered to those who cannot tolerate rifampicin such as people with HIV/AIDS on anti-retrovirals [11]. Therefore, its use is less common as compared to rifampicin. Rifapentine is an antibiotic which is used in the treatment of tuberculosis in combination with other antibiotics [5]. Like in active tuberculosis it is given together with other anti-tuberculosis medications. Rifapentine possess a higher rate of hepatotoxicity. Its use is also not as common as rifampicin. However, the diagnosis of RIF resistant has been traditionally difficult, because it requires sophisticated biosafety and laboratory infrastructure, which is hardly available [4,58].

The crystal structures of both these antibiotics indicate a heterocyclic structure containing a napthoquinone core which is spanned by an aliphatic ansa chain. The ansa bridge and the naphthol ring form a cavity like structure with four critical hydroxyl groups lying alongside the ring which form hydrogen bonds with amino acid residues on the protein during the inhibitory binding of bacterial RNA polymerase. We presumed that a similar binding mechanism should exist with the composite material prepared in this work with a larger steric hindrance coming from the additional cyclopentane group in RIP blocking the cavity and the access to the hydroxyl groups. In order to confirm this presumption, we selected another drug having similar size and molar mass, but differ significantly in the structure from RIF, i.e., rifabutin (RIB) which is also used to treat tuberculosis, but only in those patients who cannot tolerate RIF due to a compromised immune system due to HIV infections. Again, the crystal structure indicates that there are no accessible hydroxyl groups forming hydrogen bonds, so the mechanism of action is somewhat different.

The sensor responses were obtained for 0.5 mM solutions of both of the selected drugs, in addition to RIF, and the resultant sensor profiles are shown in Fig. 6A. Evidently, the MWCNTs/Bi_2WO_6 nanocomposite showed almost no response to RIB as compared to RIF, which produced a normalized frequency shift of 100 Hz. Contrarily, RIP showed some binding effect but still much smaller than RIF due to presumed steric hindrance in binding. This indicates that the MWCNTs/Bi_2WO_6 nanocomposite can provide higher selectivity for RIF even in the presence of compounds that possess similar characteristics in functional groups, shape, and size while only differing in some specific binding capabilities. Undoubtedly, this extraordinary selectivity is generated by the MWCNTs/Bi_2WO_6 synergistic effects in the first place. However, to bring our understanding of the mechanism further, we investigated the recognition process using HATR-IR by preparing three different suspensions of RIB, RIP, and RIF MWCNTs/Bi_2WO_6 nanocomposite

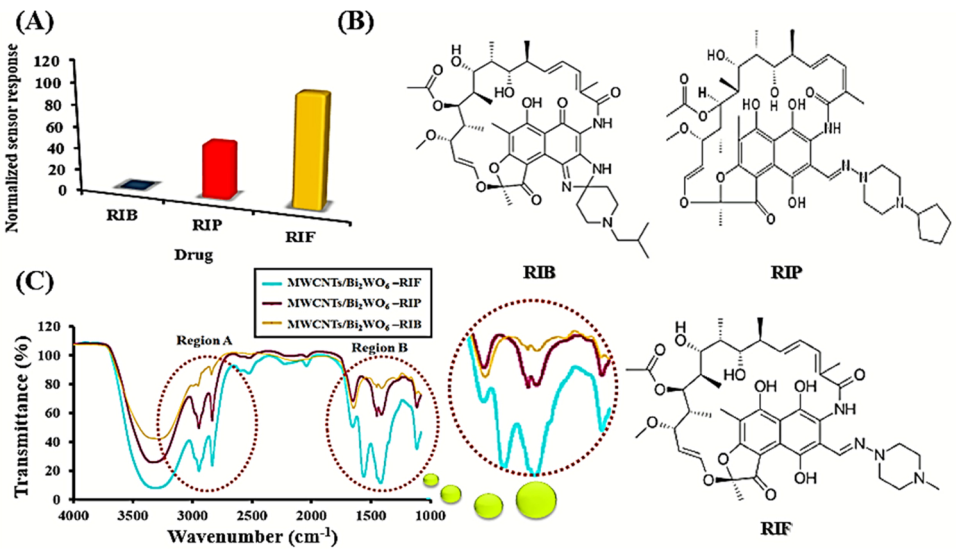

Fig. 6. (A) Selectivity profiles; comparison of the responses toward some potential interfering agents on the MWCNTs/Bi_2WO_6 modified QCM devices, (B) RIF and its structural analogs; RIF = rifampicin; RIB = rifabutin, and RIP = rifapentine and (C) comparison of HATR-IR spectra of MWCNTs/Bi_2WO_6-RIF, MWCNTs/Bi_2WO_6-RIP and MWCNTs/Bi_2WO_6-RIB {Region A is indicating OH, C—C bonding while region B is for C═O}.

(0.4 mg mL^{-1} each). Their respective profiles are displayed in Fig. 6C. If we observe the regions of major changes as the result of corresponding interactions of the drugs with MWCNTs/Bi_2WO_6, these were found to be the greatest of the three for the RIF drug. In FTIR, MWCNTs/Bi_2WO_6-RIB exhibited a distinct double peak at 1734 and 1712 cm^{-1} due to ester C═O and ketone C O stretch respectively, however, in MWCNTs/Bi_2WO_6-RIF and MWCNTs/Bi_2WO_6-RIP there was a single peak by acetyl C O at 1725 cm^{-1}. The absorption band in RIB showed a peak at 3480 cm^{-1} that is due to O—H stretch, ansa chain is not present in RIB, whereas in MWCNTs/Bi_2WO_6-RIF and MWCNTs/Bi_2WO_6-RIP it was a broad band due to the ansa OH over the range of 3565–3150 cm^{-1}. The results have been summarized in Table S1. The OH and the C—C network are influenced by the interaction of the composite and this region is majorly influenced in the case of RIF. Obviously, this observation confirms the strong interaction between the RIF and composite. In other words, the binding preference of the RIF has mainly worked as recognition directive forces. This can be regarded as extraordinary specificity when we used the affinity material for the detection of RIF in comparison to other drugs. Imprinted materials are especially a popular choice to impart selectivity [59]. However, this shows that by tuning the nature of the substrate and developing material synergy of the nanomaterials, we can develop a transducer material for selective detection. Moreover, such selective non-specific binding can also lead to sensor array designs for the detection of multiple drugs simultaneously by applying modern data analysis and even artificial intelligence techniques which are getting popular in sensor science. Therefore, this study opens a new avenue whereas affinity based sensors can be intelligently manipulated for the selective detection of complex analytes, especially biomolecules that contain a mixture of various functional groups. Since MWCNTs/Bi_2WO_6 nanocomposite rely on the affinity between the RIF and composite, and the resulting selectivity should be influenced by the nature and extent of these interactions. For a better understanding, further studies can be targeted to investigate and understand only the binding mechanisms in detail.

3.6. Real sample

The proper and true metabolization of RIF is not possible due to its bioavailability. RIF dosage is based on an individualized clinical process using the best judgment of a physician trained to administer this antibiotic. In fact, due to the differences in the pharmacokinetics RIF and its bioavailability among different people, development of the therapeutic drug monitoring based on rapid and reliable analytical methods is particularly important [62–64]. They should determine the RIF concentration to individualize doses for achieving efficient treatment. However, its assessment in the human serum can be carried out by standard addition method. The capability of the sensor was evaluated by analyzing RIF in spiked urine samples. These were originally obtained from three healthy volunteers. Sample collection was performed according to institutional ethic approval and informed consent was obtained from the volunteers. Urine samples were stored in a refrigerator immediately after its collection. For analysis, 5.0 mL of the sample was centrifuged for 15 min at 2000 rpm. The aliquot amounts of RIF were added to urine samples and the spiked amount was chosen from the linear part of the calibration curve. To eliminate the system error, the net response was calculated from the difference of blank medium (sample having no RIF) to the test solution (spiked with RIF), with reference to the standard curve. Each measurement was employed in triplicate by the standard addition method (n = 3) and the analysis data were summarized in Table 2. A recovery study was performed and values ranged from 84 to 101% indicating The MWCNTs-Bi_2WO_6 nanocomposite modified QCM devices offers the satisfactory recoveries for the determination of RIF in biological samples. However, here it is worth to mention that the response of the QCM critically depends on environmental factors and the viscosity and conductivity of the real reaction solution due to the non-mass effect on the resonance frequency; therefore, recoveries may vary with the type of biological specimen and sample pre-treatments methods. However, if we consider that only a small proportion of the dose administrated to the patient is excreted unchanged in the urine, i.e. 15–25%. The total quantity found can be determined by utilizing corresponding calibration curve equations for spiked RIF amount in urine [65,66]. Moreover,

Table 2
Recovery results of RIF determination at MWCNTs-Bi_2WO_6 nanocomposite modified QCM devices in human urine sample (n = 3).

Sample	Spiked (μM)	Found[a] (μM)	Recovery (%)
1	1	1.01 ± 4.1	101
	10	9.7 ± 3.3	97
	100	101.3 ± 2.1	101.3
2	1	0.84 ± 2.9	84
	10	8.7 ± 3.2	87
	100	90.9 ± 1.7	90.9
3	1	0.83 ± 2.2	88.3
	10	8.48 ± 2.2	84.8
	100	87 ± 1.8	87

[a] Average of three determinations.

implementation of this work for clinical purpose needs further investigations and optimization of the procedures.

4. Conclusion

In summary, we developed MWCNTs/Bi_2WO_6 nanocomposite as a sensor coating for the mass-sensitive detection of rifampicin. Morphological and structural characterization showed that the prepared composite consisted of an intricate network of carbon tubes embracing nanosheets of Bi_2WO_6. This nanocomposite was employed as a transducer layer for RIF onto the QCM sensor and multiple studies were directed to bring out the sensing characteristics of the material as well as to have a preliminary understanding of the selectivity. The developed sensor showed high sensitivity toward rifampicin with a detection limit of 0.16 µM while having excellent reproducibility and stability. These responses were significantly higher than the individual components of the composite demonstrating that a synergy effect was generated by the developed nanosheets. Additionally, MWCNTs/Bi_2WO_6 nanocomposite coated QCM sensors bear high specificity toward RIF as compared to the two drugs systematically chosen to provide an interference effect as well as some understanding of the binding process. The novel morphology of the MWCNTs/Bi_2WO_6 nanocomposite and the remarkable sensor characteristics of the coated QCM opens up a new platform where, synergistic effects of nanomaterials and their mutual interactions with the analyte, can be exploited for the detection of biomolecules.

Acknowledgement

This research was jointly supported by the International Foundation for Science (IFS) and the Organization of the Islamic Cooperation's (OIC) Standing Committee on Scientific and Technological Cooperation (COMSTECH) via project no. E-5659.

Appendix A. Supplementary data

Supplementary data associated with this article can be found, in the online version, at https://doi.org/10.1016/j.jhazmat.2019.03.054.

References

[1] M.E. Vance, Kuiken, E.P. Vejerano, S.P. McGinnis, M.F. Hochella Jr., D. Rejeski, M.S. Hull, Nanotechnology in the real world: redeveloping the nanomaterial consumer products inventory, Beilstein J. Nanotechnol. 6 (2015) 1769–1780.
[2] WH Organization, Tracking Universal Health Coverage: First Global Monitoring Report, World Health Organization, 2015.
[3] S.R. Kaplan, J. Topal, L. Sosa, M. Malinis, A. Huttner, A. Malhotra, G. Friedland, A patient with central nervous system tuberculomas and a history of disseminated multi-drug-resistant tuberculosis, Int. J. Tuberc. Lung Dis. 10 (2018) 9–16.
[4] E.S. Björnsson, Drug-induced liver injury: an overview over the most critical compounds, Arch. Toxicol. 89 (2015) 327–334.
[5] B. Williamson, K.E. Dooley, Y. Zhang, D. Back, A. Owen, Induction of influx and efflux transporters and cytochrome P450 3A4 in primary human hepatocytes by rifampicin, rifabutin and rifapentine, Antimicrob. Agents Chemother. (2013) AAC. 01124-01113.
[6] Y. Hu, A. Liu, F. Ortega-Muro, L. Alameda-Martin, D. Mitchison, A. Coates, High-dose rifampicin kills persisters, shortens treatment duration, and reduces relapse rate in vitro and in vivo, Front. Microbiol. 6 (2015) 641.
[7] P. Alifano, C. Palumbo, D. Pasanisi, A. Talà, Rifampicin-resistance, rpoB polymorphism and RNA polymerase genetic engineering, J. Biotechnol. 202 (2015) 60–77.
[8] J. Millard, C. Ugarte-Gil, D. Moore, Multidrug resistant tuberculosis, BMJ 350 (2015) h882.
[9] L. Lacerda, A.L. Parize, V. Fávere, M.C.M. Laranjeira, H.K. Stulzer, Development and evaluation of pH-sensitive sodium alginate/chitosan microparticles containing the antituberculosis drug rifampicin, Mater. Sci. Eng. C 39 (2014) 161–167.
[10] L. Asturias-Arribas, M.A. Alonso-Lomillo, O. Domínguez-Renedo, M.J. Arcos-Martínez, Sensitive and selective cocaine electrochemical detection using disposable sensors, Anal. Chim. Acta 834 (2014) 30–36.
[11] A. Kohli, G. Bashir, A. Fatima, A. Jan, J. Ahmad, Rapid drug-susceptibility testing of *Mycobacterium tuberculosis* clinical isolates to first-line antitubercular drugs by nitrate reductase assay: a comparison with proportion method, Int. J. Mycobacteriol. 5 (2016) 469–474.
[12] Y. Matsuda, S. Shibayama, K. Uete, H. Yamaguchi, T. Niimi, Electric conductive pattern element fabricated using commercial inkjet printer for paper-based analytical devices, Anal. Chem. 87 (2015) 5762–5765.
[13] Y. Jiang, J.L. Carvalho-de-Souza, R.C. Wong, Z. Luo, D. Isheim, X. Zuo, A.W. Nicholls, I.W. Jung, J. Yue, D.-J. Liu, Heterogeneous silicon mesostructures for lipid-supported bioelectric interfaces, Nat. Mater. 15 (2016) 1023–1030.
[14] D. Liu, H. Zhang, F. Fontana, J.T. Hirvonen, H.A. Santos, Microfluidic-assisted fabrication of carriers for controlled drug delivery, Lab Chip 17 (2017) 1856–1883.
[15] H. Djani, P. Hermet, P. Ghosez, First-principles characterization of the P21ab ferroelectric phase of Aurivillius Bi_2WO_6, J. Phys. Chem. C 118 (2014) 13514–13524.
[16] H.H. Sønsteby, H. Fjellvåg, O. Nilsen, Functional perovskites by atomic layer deposition – an overview, Adv. Mater. Interfaces (2017) 1–15.
[17] W. Wang, X. Shen, W. Wang, X. Guan, Y. Yao, Y. Wang, R. Yu, The evolution of microstructure and magnetic properties of the bismuth layer compounds with cobalt ions substitution, Inorg. Chem. 56 (2017) 3207–3213.
[18] L. Liao, Q. Zhang, Z. Su, Z. Zhao, Y. Wang, Y. Li, X. Lu, D. Wei, G. Feng, Q. Yu, Efficient solar water-splitting using a nanocrystalline CoO photocatalyst, Nat. Nanotechnol. 9 (2014) 69–73.
[19] N.D. Phu, L.H. Hoang, P.-C. Guo, X.-B. Chen, W.C. Chou, Study of photocatalytic activities of Bi_2WO_6/$BiVO_4$ nanocomposite, J. Sol-Gel Sci. Technol. 83 (2017) 640–646.
[20] D.-P. Song, Y. Lin, Y. Gai, N.S. Colella, C. Li, X.-H. Liu, S. Gido, J.J. Watkins, Controlled supramolecular self-assembly of large nanoparticles in amphiphilic brush block copolymers, J. Am. Chem. Soc. 137 (2015) 3771–3774.
[21] Y.P. Bhoi, D.P. Rout, B. Mishra, Photocatalytic chemoselective aerobic oxidation of thiols to disulfides catalyzed by combustion synthesized bismuth tungstate nanoparticles in aqueous Media, J. Cluster Sci. 27 (2016) 267–284.
[22] P.L. Rocha, D.A.B. Barbosa, J.R. de Oliveira Lima, G.M.P. Prazeres, C.W. de Araujo Paschoal, M.S. Li, E. Longo, A.P. Maciel, M.A.P. Almeida, Enhancement of symmetry-induced photoluminescence in bismuth tungstate microcrystals, Mater. Lett. 184 (2016) 298–300.
[23] L. Liang, F. Lei, S. Gao, Y. Sun, X. Jiao, J. Wu, S. Qamar, Y. Xie, Single unit cell bismuth tungstate layers realizing robust solar CO_2 reduction to methanol, Angew. Chem. Int. Ed. 54 (2015) 13971–13974.
[24] H. Huang, K. Xiao, Y. He, T. Zhang, F. Dong, X. Du, et al., *In situ* assembly of BiOI@$Bi_{12}O_{17}Cl_2$ pn junction: charge induced unique front-lateral surfaces coupling heterostructure with high exposure of BiOI {001} active facets for robust and nonselective photocatalysis, Appl. Catal. B 199 (2016) 75–86.
[25] A. Hameed, T. Montini, V. Gombac, P. Fornasiero, Surface phases and photocatalytic activity correlation of Bi_2O_3/Bi_2O_{4-x} nanocomposite, J. Am. Chem. Soc. 130 (2008) 9658–9659.
[26] D. Yang, Z. Hou, Z. Cheng, C. Li, J. Lin, Current advances in lanthanide ion (Ln3+)-based upconversion nanomaterials for drug delivery, Chem. Soc. Rev. 44 (2015) 1416–1448.
[27] M.P. Landry, H. Ando, A.Y. Chen, J. Cao, V.I. Kottadiel, L. Chio, D. Yang, J. Dong, T.K. Lu, M.S. Strano, Single-molecule detection of protein efflux from microorganisms using fluorescent single-walled carbon nanotube sensor arrays, Nat. Nanotechnol. 12 (2017) 368–377.
[28] A. Rabti, N. Raouafi, A. Merkoçi, Bio (sensing) devices based on ferrocene-functionalized graphene and carbon nanotubes, Carbon 108 (2016) 481–514.
[29] D.-Y. Wang, M. Gong, H.-L. Chou, C.-J. Pan, H.-A. Chen, Y. Wu, M.-C. Lin, M. Guan, J. Yang, C.-W. Chen, Highly active and stable hybrid catalyst of cobalt-doped FeS_2 nanosheets–carbon nanotubes for hydrogen evolution reaction, J. Am. Chem. Soc. 137 (2015) 1587–1592.
[30] D.P. Salem, M.P. Landry, G. Bisker, J. Ahn, S. Kruss, M.S. Strano, Chirality dependent corona phase molecular recognition of DNA-wrapped carbon nanotubes, Carbon 97 (2016) 147–153.
[31] S. Cao, J. Low, J. Yu, M. Jaroniec, Polymeric photocatalysts based on graphitic carbon nitride, Adv. Mater. 27 (2015) 2150–2176.
[32] G. Huang, F. Zhang, X. Du, Y. Qin, D. Yin, L. Wang, Metal organic frameworks route to in situ insertion of multiwalled carbon nanotubes in Co_3O_4 polyhedra as anode materials for lithium-ion batteries, ACS Nano 9 (2015) 1592–1599.
[33] A. Al Faraj, A.P. Shaik, A.S. Shaik, Magnetic single-walled carbon nanotubes as efficient drug delivery nanocarriers in breast cancer murine model: noninvasive monitoring using diffusion-weighted magnetic resonance imaging as sensitive imaging biomarker, Int. J. Nanomed. 10 (2015) 157–168.
[34] K. Liew, Z. Lei, L. Zhang, Mechanical analysis of functionally graded carbon nanotube reinforced composites: a review, Compos. Struct. 120 (2015) 90–97.
[35] V.K. Thakur, M.R. Kessler, Self-healing polymer nanocomposite materials: a review, Polymer 69 (2015) 369–383.
[36] S. Zhu, Y. Song, X. Zhao, J. Shao, J. Zhang, B. Yang, The photoluminescence mechanism in carbon dots (graphene quantum dots, carbon nanodots, and polymer dots): current state and future perspective, Nano Res. 8 (2015) 355–381.
[37] W. Zhou, Y. Guo, H. Zhang, Y. Su, M. Liu, B. Dong, A highly sensitive ammonia sensor based on spinous core–shell PCL–PANI fibers, J. Mater. Sci. 52 (2017) 6554–6566.
[38] Y. Luan, D. Li, T. Wei, M. Wang, Z. Tang, J.L. Brash, H. Chen, "Hearing loss" in QCM measurement of protein adsorption to protein resistant polymer brush layers, Anal. Chem. 89 (2017) 4184–4191.
[39] A. Bearzotti, A. Macagnano, P. Papa, I. Venditti, E. Zampetti, A study of a QCM sensor based on pentacene for the detection of BTX vapors in air, Sens. Actuators B: Chem. 240 (2017) 1160–1164.
[40] L. Wang, R. Wang, H. Wang, M. Slavik, H. Wei, Y. Li, An aptamer-based PCR method coupled with magnetic immunoseparation for sensitive detection of *Salmonella typhimurium* in ground turkey, Anal. Biochem. 533 (2017) 34–40.
[41] N. Kananizadeh, C. Rice, J. Lee, K.B. Rodenhausen, D. Sekora, M. Schubert,

E. Schubert, S. Bartelt-Hunt, Y. Li, Combined quartz crystal microbalance with dissipation (QCM-D) and generalized ellipsometry (GE) to characterize the deposition of titanium dioxide nanoparticles on model rough surfaces, J. Hazard. Mater. 322 (2017) 118–128.
[42] M.D. Levi, N. Shpigel, S. Sigalov, V. Dargel, L. Daikhin, D. Aurbach, *In situ* porous structure characterization of electrodes for energy storage and conversion by EQCM-D: a review, Electrochim. Acta 232 (2017) 271–284.
[43] L. Zhang, Y. Zhu, A review of controllable synthesis and enhancement of performances of bismuth tungstate visible-light-driven photocatalysts, Catal. Sci. Technol. 2 (2012) 694–706.
[44] W.-L.W. Lee, S.-T. Huang, J.-L. Chang, J.-Y. Chen, M.-C. Cheng, C.-C. Chen, Photodegradation of CV over nanocrystalline bismuth tungstate prepared by hydrothermal synthesis, J. Mol. Catal. A: Chem. 361 (2012) 80–90.
[45] Y. Tian, L. Zhang, J. Zhang, A superior visible light-driven photocatalyst: europium-doped bismuth tungstate hierarchical microspheres, J. Alloys Compd. 537 (2012) 24–28.
[46] M. Chen, W. Chu, Photocatalytic degradation and decomposition mechanism of fluoroquinolones norfloxacin over bismuth tungstate: experiment and mathematic model, Appl. Catal. B 168 (2015) 175–182.
[47] Y.P. Bhoi, D.P. Rout, B. Mishra, Photocatalytic chemoselective aerobic oxidation of thiols to disulfides catalyzed by combustion synthesized bismuth tungstate nanoparticles in aqueous media, J. Cluster Sci. 27 (2016) 267–284.
[48] B. Cao, W. Cai, Y. Li, F. Sun, L. Zhang, Ultraviolet-light-emitting ZnO nanosheets prepared by a chemical bath deposition method, Nanotechnology 16 (2005) 1734.
[49] B. Zheng, Y. Chen, Z. Wang, F. Qi, Z. Huang, X. Hao, P. Li, W. Zhang, Y. Li, Vertically oriented few-layered HfS_2 nanosheets: growth mechanism and optical properties, 2D Mater. 3 (2016) 035024.
[50] A.D. Moghadam, E. Omrani, P.L. Menezes, P.K. Rohatgi, Mechanical and tribological properties of self-lubricating metal matrix nanocomposite reinforced by carbon nanotubes (CNTs) and graphene – a review, Compos. Part B: Eng. 77 (2015) 402–420.
[51] Y. Tian, G. Hua, W. Xu, N. Li, M. Fang, L. Zhang, Bismuth tungstate nano/microstructures: controllable morphologies, growth mechanism and photocatalytic properties, J. Alloys Compd. 509 (2011) 724–730.
[52] A. Munawar, M.A. Tahir, A. Shaheen, P.A. Lieberzeit, W.S. Khan, S.Z. Bajwa, Investigating nanohybrid material based on 3D CNTs@Cu nanoparticle composite and imprinted polymer for highly selective detection of chloramphenicol, J. Hazard. Mater. 342 (2018) 96–106.
[53] N. Campbell, Bicyclic compounds containing a pyridine ring: quinoline and its derivatives, Rodd's Chemistry of Carbon Compounds, second edition, Elsevier, 2008, pp. 231–356.
[54] B. Yu, L.N. He, Upgrading carbon dioxide by incorporation into heterocycles, ChemSusChem 8 (2015) 52–62.
[55] G. Ruggeri, S. Takahama, Development of chemoinformatic tools to enumerate functional groups in molecules for organic aerosol characterization, Atmos. Chem. Phys. 16 (2016) 4401–4422.
[56] M.A.A. Lomillo, O.D. Renedo, M.J.A. Martínez, Optimization of a cyclodextrin-based sensor for rifampicin monitoring, Electrochim. Acta 50 (2005) 1807–1811.
[57] P. Daneshgar, P. Norouzi, F. Dousty, M.R. Ganjali, A.A. Moosavi-Movahedi, Dysprosium hydroxide nanowires modified electrode for determination of rifampicin drug in human urine and capsules by adsorptive square wave voltammetry, Curr. Pharm. Anal. 5 (2009) 246–255.
[58] S. Rastgar, S. Shahrokhian, Nickel hydroxide nanoparticles-reduced graphene oxide nanosheets film: layer-by-layer electrochemical preparation, characterization and rifampicin sensory application, Talanta 119 (2014) 156–163.
[59] Y. Hahn, S. Shin, Electrochemical behavior and differential pulse polarographic determination of rifampicin in the pharmaceutical preparations, Arch. Pharmacal Res. 24 (2001) 100.
[60] S. Amidi, Y.H. Ardakani, M. Amiri-Aref, E. Ranjbari, Z. Sepehri, H. Bagheri, Sensitive electrochemical determination of rifampicin using gold nanoparticles/poly-melamine nanocomposite, RSC Adv. 7 (2017) 40111–40118.
[61] J. Wackerlig, R. Schirhagl, Applications of molecularly imprinted polymer nanoparticles and their advances toward industrial use: a review, Anal. Chem. 88 (2016) 250–261.
[62] S.D. Lawn, M.P. Nicol, Xpert® MTB/RIF assay: development, evaluation and implementation of a new rapid molecular diagnostic for tuberculosis and rifampicin resistance, Future Microbiol. 6 (2011) 1067–1082.
[63] E. Ohnhaus, B. Park, Measurement of urinary 6-β-hydroxycortisol excretion as an in vivo parameter in the clinical assessment of the microsomal enzyme-inducing capacity of antipyrine, phenobarbitone and rifampicin, Eur. J. Clin. Pharmacol. 15 (1979) 139–145.
[64] J.J. Wilkins, R.M. Savic, M.O. Karlsson, G. Langdon, H. McIlleron, G. Pillai, P.J. Smith, U.S. Simonsson, Population pharmacokinetics of rifampin in pulmonary tuberculosis patients, including a semimechanistic model to describe variable absorption, Antimicrob. Agents Chemother. 52 (2008) 2138–2148.
[65] C. Shishoo, S. Shah, I. Rathod, S. Savale, M. Vora, Impaired bioavailability of rifampicin in presence of isoniazid from fixed dose combination (FDC) formulation, Int. J. Pharm. 228 (2001) 53–67.
[66] G. Ellard, P. Fourie, Rifampicin bioavailability: a review of its pharmacology and the chemotherapeutic necessity for ensuring optimal absorption, Int. J. Tuberc. Lung Dis. 3 (1999) 301–308.